Evaluation of 4-D reaction integrals via double application of the divergence theorem

Evaluation of 4-D Reaction Integrals via Double Application of the Divergence Theorem

J. Rivero, F. Vipiana, *Senior Member, IEEE*, D. R. Wilton, *Life Fellow, IEEE*, W. A. Johnson, *Senior Member, IEEE*

***Abstract*—The use of the Method of Moments to solve surface integral equations is one of the most popular numerical techniques in electromagnetic modeling and analysis. This method requires the accurate and efficient numerical evaluation of iterated surface integrals over both source and testing domains.**

In this paper we propose a scheme for evaluating these 4-D interaction integrals between pairs of arbitrarily positioned and oriented elements. The approach is based on applying the surface divergence theorem twice, once on the source and once on the test domain. When the integrations are reordered as two outer contour integrals plus two inner radial integrals, the initial radial integrations provide significant smoothing of the underlying singular integrands. The method is numerically validated for static and dynamic kernels arising in the Electric Field Integral Equation (EFIE), i.e., for kernels with $1/R$ singularities, and linear basis functions. The proposed formula to evaluate 4-D reaction integrals can be extended to different kernels and to different elements, e.g., to curved or volumetric elements, and to basis functions of higher order.

***Index Terms*—integral equations, moment methods, numerical analysis, singular integrals.**

I. Introduction

Surface integral equations (SIEs) have established themselves as the principal technique to model geometrically complex objects such as naval, aerospace, and satellite structures with unknowns confined to body surfaces. The rigorous solution of radiation and scattering problems using SIEs requires the accurate and efficient numerical evaluation of double surface reaction integrals. Recently, several methods for the integration of reaction integrals in moment method solutions have been proposed to handle different kernels on flat and curved triangular elements [1]. The approach is based on an interchange of integration order in order to first perform radial integrations for the source and observation point integrals. The resulting integrals are evaluated by analytical, numerical, and hybrid schemes [2]–[5]. However, they have generally been limited to the treatment only of self-interacting, edge-adjacent, or vertex-adjacent elements, and to well-shaped (i.e., nearly equilateral) triangular element pairs.

In the present paper, we apply the surface divergence theorem twice to the 4-D reaction integrals for arbitrarily located elements and $1/R$ singular kernels, where $R = |\mathbf{r} - \mathbf{r}'|$ and $\mathbf{r}$ and $\mathbf{r}'$ are observation and source points, respectively. The authors first proposed the double application of the divergence theorem to 4-D reaction integrals, but only for the case of co-planar elements [6]. The surface divergence theorem has previously been used, for example in [7], to evaluate singular integrals in the source domain, but its application to the integrals defined over the test domain has been limited to ad hoc analytical or semi-analytical evaluations for 4-D static reaction integrals on planar domains [8], [9]. In [10] an extension of [7] is presented to evaluate term-by-term a truncated power series for the 4-D reaction integrals for the EFIE kernel with linear basis functions.

Here, by contrast, the divergence theorem is applied directly in the physical domains for both the source and observation point integrations, yielding a novel, general expression for the reaction between elements with arbitrary location, kernels, and basis functions. As in [1], the resulting 4-D surface integral is expressed as two radial integrals in combination with two contour integrals over source and observation point domains. The radial integrations are well-behaved for polygonal domains and the integral domains are not parametrically mapped, as in [1], thus eliminating restrictions to well-shaped, touching elements. In this sense, the scheme is quite general, i.e., is not limited to well-shaped elements nor to ad-hoc treatments of self-terms, or edge- or vertex-adjacent geometries.

The paper is organized as follows. In Sect. II, the proposed formula for 4-D reaction integrals between arbitrarily located elements is derived. Morover the section explores two different projections developed for mapping observation points to a local origin in the plane of the source points (and vice versa) for applying the divergence theorem. Sect. III proposes variable transformations to improve the numerical evaluation of the inner radial integral and the contour integrals. Numerical results are presented in Sect. IV, and Sect. V contains conclusions. In [11], some preliminary results related to the proposed approach were presented.

II. Reaction Integral for an Element Pair

Our goal is to perform accurate and efficient numerical evaluation of 4-D integrals of the form

$$I_{T,T'} = \int_T \int_{T'} F(\mathbf{r}, \mathbf{r}')\, dS' dS. \tag{1}$$

Manuscript received xxxxxx x, 2017. This work was supported in part by Junta de Extremadura and the European Social Fund (EFS).

J. Rivero was with the Department of Computers and Comunications, Escuela Politécnica de Cáceres, Universidad de Extremadura, 10003 Cáceres, Spain. He is now with the Department of Electronics and Telecommunications, Politecnico di Torino, 10129 Torino, Italy (email: javier.rivero@polito.it).

F. Vipiana is with the Department of Electronics and Telecommunications, Politecnico di Torino, 10129 Torino, Italy (email: francesca.vipiana@polito.it).

D. R. Wilton is with the Department of Electrical and Computer Engineering, University of Houston, Houston, TX 77204-4005 USA (email: wilton@uh.edu).

W. A. Johnson is an electromagnetics consultant in Albuquerque, NM 87123, USA (e-mail: w.johnson24@comcast.net).

Color versions of one or more of the figures in this communication are available online at http://ieeexplore.ieee.org.

Digital Object Identifier xxxxxxxxxxxxxxxxxxxx

Typically, $F(\mathbf{r},\mathbf{r}')$ takes the form

$$F(\mathbf{r},\mathbf{r}') = t(\mathbf{r})g(\mathbf{r},\mathbf{r}')b(\mathbf{r}'), \tag{2}$$

where $t(\mathbf{r})$ is either a scalar or a vector component of a testing function, $b(\mathbf{r}')$ is similarly defined for a basis function, $g(\mathbf{r},\mathbf{r}')$ is either a scalar, or a scalar component of a vector or dyadic Green's function, and T and T' are the definition domains of the testing and basis functions respectively.

The most common approach for evaluating (1) is to first evaluate the inner (singular) integral over T', then, treating the resulting integrand as no longer singular, evaluate the outer integral over T via a standard Gauss quadrature scheme (see e.g. [12]–[14]). Here, instead, the surface divergence theorem is applied in the physical domain to both the test and source integrals of the 4-D reaction integrals.

Consider first the inner surface integral (on the primed variables) over the source domain T' with unit normal vector $\hat{\mathbf{n}}'$ and $\mathbf{r}$ fixed:

$$I_{T'} = \int_{T'} F(\mathbf{r},\mathbf{r}')\, dS'. \tag{3}$$

Similar to the approach in [6], the surface divergence theorem is applied to (3), resulting in

$$I_{T'} = \int_{T'} \nabla'\cdot\mathbf{H}\, dS' = \oint_{C'} \mathbf{H}(\mathbf{r},\mathbf{r}'_{C'})\cdot\hat{\mathbf{u}}'\, dC', \tag{4}$$

where $\mathbf{r}'_{C'}$ is a point on the boundary C' of T', $\hat{\mathbf{u}}'$ is the external unit normal to C' in the plane S' containing source domain T' (see Fig. 1), and

$$\mathbf{H}(\mathbf{r},\mathbf{r}'_{C'}) = \frac{\hat{\mathbf{D}}'}{D'_{C'}} \int_0^{D'_{C'}} F(\mathbf{r},\mathbf{r}')D'dD', \tag{5}$$

with $\mathbf{r}' = \mathbf{r}^0 + D'\hat{\mathbf{D}}'$, $\hat{\mathbf{D}}' = (\mathbf{r}'_{C'} - \mathbf{r}^0)/D'_{C'}$, $0 < D' < D'_{C'}$, $D'_{C'} = |\mathbf{r}'_{C'} - \mathbf{r}^0|$. $\mathbf{H}(\mathbf{r},\mathbf{r}'_{C'})$ is assumed to have only a radial component with respect to $\mathbf{r}^0$. The point $\mathbf{r}^0$ is an arbitrarily-located local polar coordinate origin in the plane S' used to apply the divergence theorem; a different origin may be associated with each value of $\mathbf{r}$, but should be independent of $\mathbf{r}'_{C'}$. We can express this as a mapping, $\mathbf{r}^0 = \mathcal{T}^-(\mathbf{r})$, where the negative sign in $\mathcal{T}^-$ means that values $\mathbf{r}$ in the observation plane are mapped to the source plane, i.e., in the direction of decreasing tilt angle β between planes S (containing T) and S' (see Fig. 2).

Next, we integrate over the test domain, yielding the following double surface integral:

$$\begin{aligned} I_{T,T'} &= \int_T \int_{T'} F(\mathbf{r},\mathbf{r}')dS'dS \\ &= \oint_{C'} \hat{\mathbf{u}}'\cdot \int_T \frac{\hat{\mathbf{D}}'}{D'_{C'}} \int_0^{D'_{C'}} F(\mathbf{r},\mathbf{r}')D'dD'dS\, dC', \end{aligned} \tag{6}$$

where the interchange of integration order is permitted by the independence of the observation and source coordinate variables and their associated domains. Applying the surface divergence theorem once more to the inner surface integral of (6) and reordering the integration order once more, we obtain

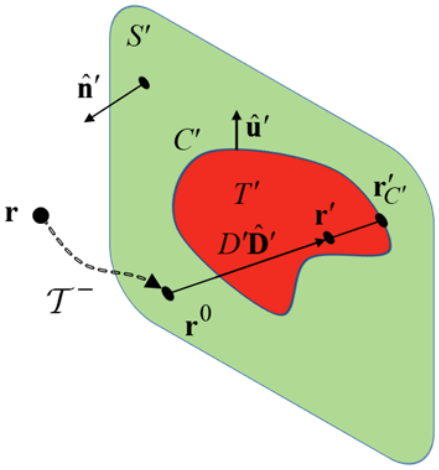

Fig. 1. Radial path contributions to integral (5) in the source plane, and geometrical definitions.

the following general formula:

$$I_{T,T'} = \oint_C \oint_{C'} \frac{\hat{\mathbf{u}}\cdot\hat{\mathbf{D}}}{D_C} \int_0^{D_C} \frac{\hat{\mathbf{u}}'\cdot\hat{\mathbf{D}}'}{D'_{C'}} \int_0^{D'_{C'}} F(\mathbf{r},\mathbf{r}')D'dD'DdD\, dC'dC, \tag{7}$$

where C is the boundary of T, $\hat{\mathbf{u}}$ is the external unit normal to C in the test plane S, $\mathbf{r} = \mathbf{r}'^0_{C'} + D\hat{\mathbf{D}}$, where $\hat{\mathbf{D}} = (\mathbf{r}_C - \mathbf{r}'^0_{C'})/D_C$ and $0 \le D \le D_C$, with $D_C = |\mathbf{r}_C - \mathbf{r}'^0_{C'}|$ and with $\mathbf{r}_C$ a point on the boundary of T. The mapping $\mathbf{r}'^0_{C'} = \mathcal{T}^+(\mathbf{r}'_{C'})$ transforms a point on C' to a local polar coordinate origin $\mathbf{r}'^0_{C'}$ in the plane S. Note that Eq. (6) can also be interpreted as integration in polar coordinates. This interpretation, however, applies only to the *first* use of the divergence theorem but not to the *second* in Eq. (7).

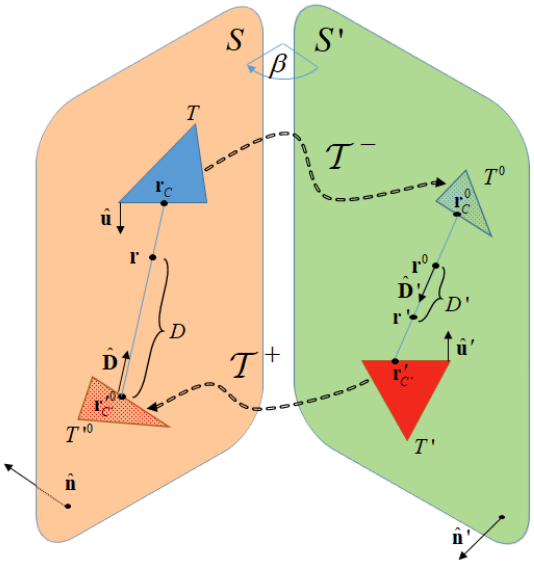

Fig. 2. Geometrical definitions for source and test triangles (T' and T) with their corresponding projections onto the test and source planes, respectively.

For general polygonal domains, such as for the two triangles

T and T' illustrated in Fig. 2, the contour integrals can be evaluated by considering all the contributions resulting from interacting pairs of source and test edges forming the polygons' boundaries. Thus evaluation of (7) reduces to evaluating contributions such as

$$I_{\Delta C,\Delta C'} = \int_{\rho_L}^{\rho_U}\int_{\rho'_L}^{\rho'_U} \frac{\hat{\mathbf{u}}\cdot\hat{\mathbf{D}}}{D_C}\int_0^{D_C}\frac{\hat{\mathbf{u}}'\cdot\hat{\mathbf{D}}'}{D'_{C'}}\int_0^{D'_{C'}} F(\mathbf{r},\mathbf{r}')D'dD'DdD\,d\rho' d\rho \tag{8}$$

that represent the interaction between segment pairs ΔC and $\Delta C'$, parameterized by ρ and ρ' respectively, with ρ_L and ρ_U as lower and upper limits, respectively, of the ΔC integral and similarly for corresponding primed quantities. Without loss of generality, in the following we assume that the edges ΔC and $\Delta C'$ belong to the triangles T and T', respectively. Note that the interaction between edges will vanish if a line segment's projection in the other plane is collinear with the edge in that plane (see Fig. 3) since at least one of the dot products in (8), $\hat{\mathbf{u}}\cdot\hat{\mathbf{D}}$ or $\hat{\mathbf{u}}'\cdot\hat{\mathbf{D}}'$, vanishes. For non-collinear projected edges, straightforward Gauss-Legendre quadrature of sufficiently high order may be able to reach a desired level of accuracy, but for further accuracy, or simply to improve the accuracy of low-order quadrature schemes, it is suggested to transform the integrals (8) into faster converging forms. A more detailed description of such transforms appears in Sect. III.

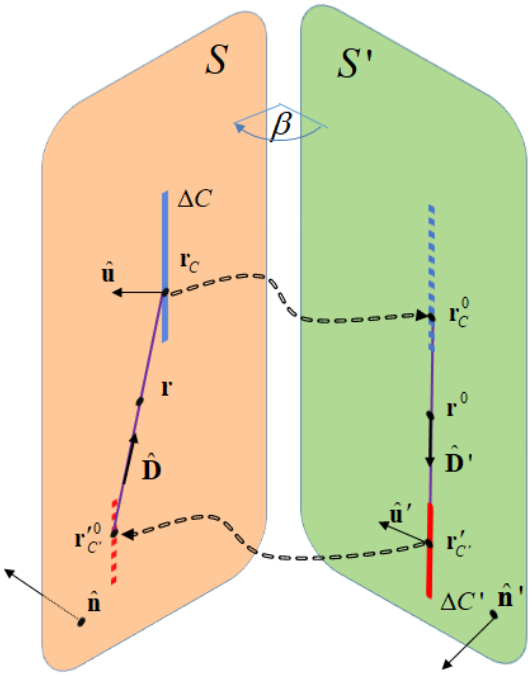

Fig. 3. Example of a pair of edges where the line segment's projection in the source plane is collinear with the edge in that plane.

To evaluate the integral in (8), we need to introduce a projection scheme between the points in the observation and source planes respectively. Not all projection schemes are valid, nor are all valid ones unique. Here we propose two particularly simple and useful schemes. The first is an *orthogonal projection* and the second is a *rotational projection*.

A. Orthogonal projection

One possible orthogonal projection is to project a point along the unit vector normal to the plane in which the point is located. That is, we extend a line from the point $\mathbf{r}$ in S along the direction of the unit normal vector $\hat{\mathbf{n}}$ to its intersection with S' at the projected point $\mathbf{r}^0$. This simple projection, however, has the drawback that no intersection occurs when the planes S and S' are orthogonal. Instead, the general case can be handled by projecting $\mathbf{r}$ along the direction of the unit normal vector $\hat{\mathbf{n}}'$ to an intersection point $\mathbf{r}^0$ in S', as shown in Fig. 4. Similarly, the point $\mathbf{r}'_{C'} \in S'$ is projected to $\mathbf{r}'^0_{C'} \in S$ along the direction of the unit normal vector $\hat{\mathbf{n}}$. In the following, we refer to this particular projection, in which points in one plane are projected perpendicularly to the other plane, as simply the *orthogonal projection*.

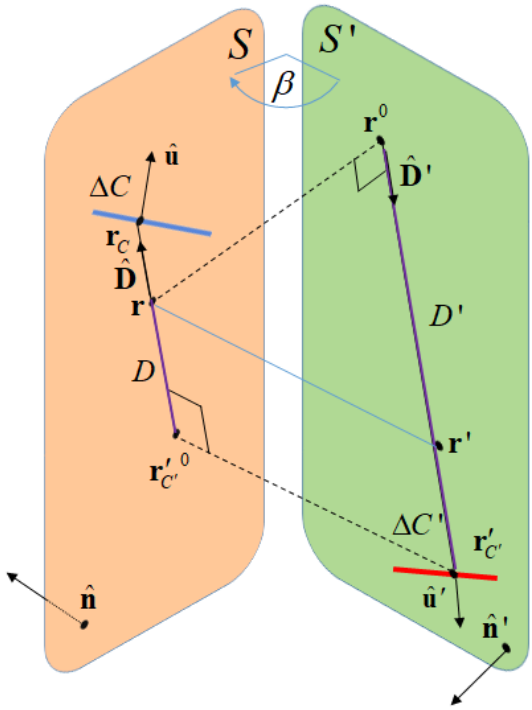

Fig. 4. Orthogonal projection.

Mathematically, we locate the orthogonal projection of a point in the source plane $\mathbf{r}'_{C'} \in S'$ onto the test plane S with normal unit vector $\hat{\mathbf{n}}$ as $\mathbf{r}'^0_{C'} = \mathbf{r}'_{C'} + (\mathbf{r}_C - \mathbf{r}'_{C'})\cdot\hat{\mathbf{n}}\hat{\mathbf{n}}$, where $\mathbf{r}_C$ can be any point in the test plane S, but for definiteness we choose a point on an edge used for the test edge integral. Similarly, the projection of a point in the test plane $\mathbf{r} \in S$ onto the source plane is $\mathbf{r}^0 = \mathbf{r} + (\mathbf{r}'_{C'} - \mathbf{r})\cdot\hat{\mathbf{n}}'\hat{\mathbf{n}}'$.

Although it is simple, we will not make extensive use of the orthogonal projection. Its main disadvantage is its dependence of the vector $\hat{\mathbf{D}}'$ on D, the outer radial integration variable, requiring a different source edge transform for each radial test integration point (see (8)).

B. Rotational projection

The *rotational projection* eliminates the main disadvantage of the orthogonal projection (see Sect. II-A). It has the desirable properties of continuity, invertibility, and independence of the vector $\hat{\mathbf{D}}'$ on the outer radial integral variable D, which simplifies the derivation of variable transforms to accelerate the edge integrals (see details in Sect. III-B)

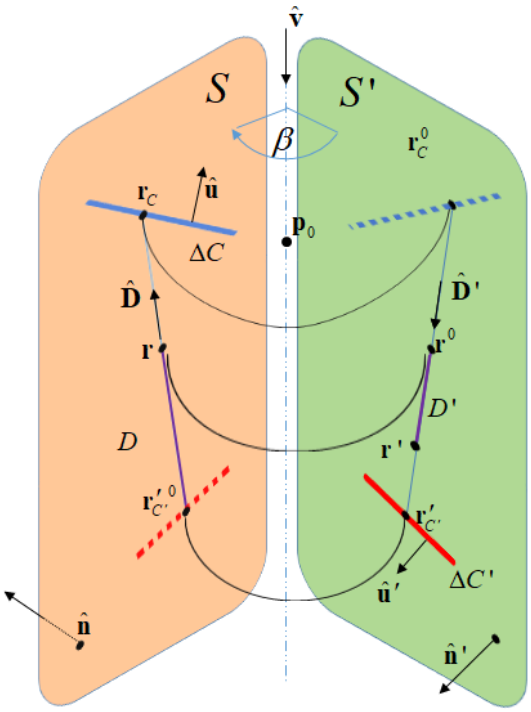

Fig. 5. Rotational Projection.

To perform the rotational projection, we define an angle β, $-\pi < \beta < \pi$, between the unit normals $\hat{\mathbf{n}}'$ and $\hat{\mathbf{n}}$, where the positive direction of β is indicated in Fig. 5. A point $\mathbf{r}_C \in S$ on the boundary of test triangle T may rotated through the angle $-\beta$ to an image point $\mathbf{r}_C^0 \in S'$. A point $\mathbf{r}'_{C'} \in S'$ on the boundary of source triangle T' may be rotated through the angle β to the point $\mathbf{r}'^0_{C'}$ on the test plane S. Indeed, the image of points of T in the plane S' and the image of T' in the plane S together with the original triangles form pairs of coplanar triangles in each plane for which the corresponding radial path quantities can be defined similar to those for the case of coplanar triangles [6]. The mathematical description of this transformation is discussed in detail in Appendix A.

Since vector $\hat{\mathbf{D}}'$ is independent of integration variable D of the outer radial integral, in the rotational projection case we can write (8) as

$$I_{\Delta C,\Delta C'} = \int_{\rho_L}^{\rho_U}\int_{\rho'_L}^{\rho'_U} \frac{(\hat{\mathbf{u}}\cdot\hat{\mathbf{D}})(\hat{\mathbf{u}}'\cdot\hat{\mathbf{D}}')}{D_C} \int_0^{D_C} \frac{1}{D'_{C'}} \int_0^{D'_{C'}} F(\mathbf{r},\mathbf{r}')D'dD'DdD\,d\rho'd\rho \tag{9}$$

In order to use the simpler form (9), in which the term involving $\hat{\mathbf{D}}'$ is removed from the radial integrals, we consider only the rotational projection in the following development.

III. Integral Transformations

To improve the convergence of the integrals (9) we next propose suitable variable transformations on the innermost radial integral and the two contour integrals.

A. Inner Radial Integral Transformation

We observe that, as in [6] (coplanar case), the integration domain of the two inner radial integrals of (9) is triangular (not to be confused with triangles T and T') in the D and D' variables, but, unlike [6], rapid variations of the factor $D'/|\mathbf{r}-\mathbf{r}'| = D'/R$ are not fully canceled since in the non-coplanar case $R \neq D'$. Hence, in this case we cannot simply implement a surface integral over the triangular radial integration domain using standard Gauss-triangle integration when the triangles are within each other's near field, where the kernel is strongly influenced by the singular or near-singular term $1/R$. Indeed, R and D' are related via the law of cosines as

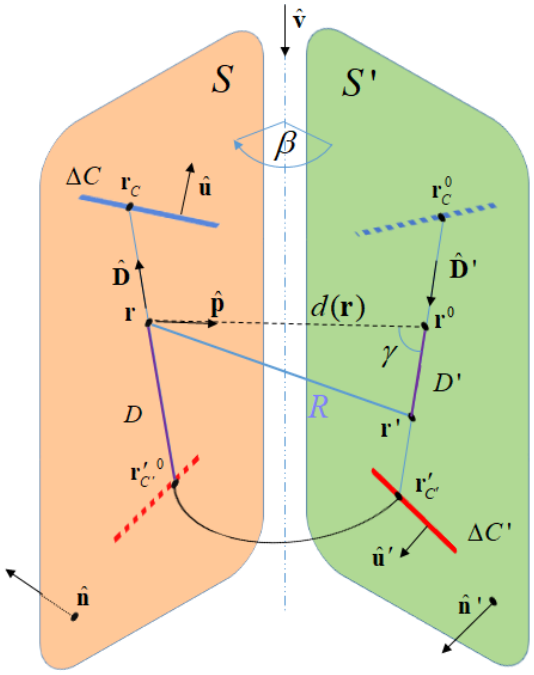

Fig. 6. Geometry for integrating radial integrals.

$$\begin{aligned} R &= \sqrt{D'^2 + d^2 - 2D'd\cos\gamma} \\ &= \sqrt{(D' - d\cos\gamma)^2 + d^2\sin^2\gamma}, \end{aligned} \tag{10}$$

where $d = d(\mathbf{r}) = |\mathbf{r^0} - \mathbf{r}|$ is the distance between the point $\mathbf{r}$ and its rotational projection $\mathbf{r^0}$, and $\cos\gamma = -\hat{\mathbf{p}}\cdot\hat{\mathbf{D}}'$, with $\hat{\mathbf{p}}$ the unit vector defining the direction to the projection point, $\hat{\mathbf{p}} = (\mathbf{r^0} - \mathbf{r})/d$. The second, completed square form of R in (10) resolves it into orthogonal components parallel and transverse to $\hat{\mathbf{D}}'$, and it is particularly useful when integrating terms involving R.

1) D'/R transform: To accelerate the convergence of the radial integral, we introduce in the following a transform (called the D'/R transform) $w'(D')$ in the inner radial integral to cancel the factor D'/R in the integrand. With this transform, the inner integral becomes

$$\int_0^{D'_{C'}} F(\mathbf{r},\mathbf{r}')D'dD' = \int_{w'(0)}^{w'(D'_{C'})} F(\mathbf{r},\mathbf{r}')D'\frac{dw'}{dw'/dD'}, \tag{11}$$

where dw'/dD' is chosen to cancel the dominant rapidly-varying term of the inner radial integrand. To estimate the kernel, we temporarily assume

$$F(\mathbf{r},\mathbf{r}') \propto \frac{1}{R}. \tag{12}$$

Substituting (12) into (11) we then have

$$\int_{w'(0)}^{w'(D'_{C'})} \frac{D'}{R}\frac{dw'}{dw'/dD'}, \tag{13}$$

suggesting the choice

$$\frac{dw'}{dD'} = \frac{D'}{R}. \tag{14}$$

Using (10), integration of (14) yields

$$w'(D') = R + d\cos\gamma \sinh^{-1}\left(\frac{D' - d\cos\gamma}{d|\sin\gamma|}\right) \tag{15}$$

and combining (13), (14), and (15) yields

$$\int_{w'(0)}^{w'(D'_{C'})} dw' = w'(D'_{C'}) - w'(0). \tag{16}$$

For constant bases and a static kernel, the result (16) is exact, i.e. since the integrand is constant, the integral can be exactly evaluated using a single sample point in the w' variable. However, when the frequency-dependent kernel phase factor or non-constant basis functions are introduced, the accuracy of the transform is significantly reduced (see Sect. IV).

2) $1/R$ transform: Due to the reduced performance of the D'/R transform for non-static kernels and non-constant bases, we propose a second transform, called the $1/R$ transform in the following, that cancels only the factor $1/R$. If we choose

$$\frac{dw'}{dD'} = \frac{1}{R} \tag{17}$$

and make use of (10), integration of (17) yields

$$w'(D') = \sinh^{-1}\left(\frac{D' - d\cos\gamma}{d|\sin\gamma|}\right). \tag{18}$$

Combining (17) with (18), Eq. (13) becomes

$$\int_{w'(0)}^{w'(D'_{C'})} D'dw'. \tag{19}$$

Since D' can be written in terms of w' as

$$D' = d|\sin\gamma|\sinh w' + d\cos\gamma, \tag{20}$$

the resulting integral (19) is easily integrated; however, the full integral (11), which may include a kernel phase factor and basis functions, must be integrated numerically. Nevertheless, the resulting integrand is sufficiently smooth that to reach machine precision requires fewer than 20 integration points (see details in Sect. IV) even when basis functions or higher order frequency terms are present. Therefore, the $1/R$ transform will be used to obtain nearly all the numerical results. For the inverse mapping, (20) can be explicitly solved for w' in terms of D'.

B. Contour Integral Transformations

To improve numerical efficiency in the evaluation of the contour integrals in (9), we also introduce transformations such that

$$\begin{aligned} I_{\Delta C,\Delta C'} &= \int_{\rho_L}^{\rho_U}\int_{\rho'_L}^{\rho'_U} (\hat{\mathbf{u}}\cdot\hat{\mathbf{D}})(\hat{\mathbf{u}}'\cdot\hat{\mathbf{D}}')\,[\,\cdot\,]\,d\rho' d\rho \\ &= \int_{u(\rho_L)}^{u(\rho_U)}\int_{u'(\rho'_L)}^{u'(\rho'_U)} (\hat{\mathbf{u}}\cdot\hat{\mathbf{D}})(\hat{\mathbf{u}}'\cdot\hat{\mathbf{D}}')\,[\,\cdot\,]\,\frac{du'}{du'/d\rho'}\frac{du}{du/d\rho}, \end{aligned} \tag{21}$$

where, to write the integral more succinctly, the brackets are assumed to include all the integrand terms of (9) except the two rapidly varying dot product factors shown explicitly; we will chose transforms such that $du'/d\rho'$ cancels variations of $\hat{\mathbf{u}}\cdot\hat{\mathbf{D}}$ and $du/d\rho$ does the same for $\hat{\mathbf{u}}'\cdot\hat{\mathbf{D}}'$.

Here, to define the geometrical parameters of the transform $du'/d\rho'$, it is convenient to (rotationally) project the source edge onto the test plane or vice versa; either way, angles and distances in the plane between the (projected) edges in the plane are preserved under rotational projection. The extended edges in the same plane then generally intersect at a point, and the edges are parameterized in terms of the distances ρ and ρ' starting at this intersection point. The angle between the extended lines is indicated by α, and all other relevant geometry quantities are shown in Fig. 7.

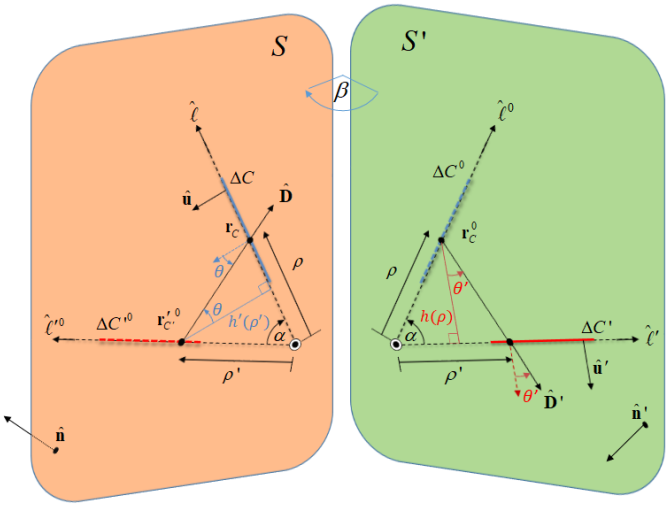

Fig. 7. Geometry definitions for integrating over a line segment pair. The solid red and blue line segments denote source and test edges $\Delta C'$ and ΔC, respectively; the dashed red and blue line segments (with labels $\Delta C'^0$ and ΔC^0, respectively) represent their projections onto the other plane.

Noting from Fig. 7 that

$$\theta = \alpha - \theta', \tag{22}$$

and that

$$\hat{\mathbf{u}}'\cdot\hat{\mathbf{D}}' = \cos\theta' = \frac{h(\rho)}{D_{CC'}} = \frac{\rho\sin\alpha}{D_{CC'}} = -\frac{\hat{\mathbf{u}}'\cdot\left(\mathbf{r}_C^0 - \mathbf{r}'_{C'}\right)}{|\mathbf{r}_C^0 - \mathbf{r}'_{C'}|}, \tag{23}$$

$$\hat{\mathbf{u}}\cdot\hat{\mathbf{D}} = -\cos\theta = -\frac{h'(\rho')}{D_{CC'}} = -\frac{\rho'\sin\alpha}{D_{CC'}} = \frac{\hat{\mathbf{u}}\cdot\left(\mathbf{r}_C - \mathbf{r}_{C'}'^0\right)}{|\mathbf{r}_C - \mathbf{r}_{C'}'^0|}, \tag{24}$$

where

$$\begin{aligned} D_{CC'} &= \left|\mathbf{r_C} - \mathbf{r}_{C'}'^0\right| = \left|\mathbf{r}_C^0 - \mathbf{r}'_{C'}\right| \\ &= \sqrt{\rho^2 + \rho'^2 - 2\rho\rho'\cos\alpha}, \end{aligned} \tag{25}$$

(21) becomes

$$\begin{aligned} &\int_{\rho_L}^{\rho_U}\int_{\rho'_L}^{\rho'_U} (\hat{\mathbf{u}}\cdot\hat{\mathbf{D}})(\hat{\mathbf{u}}'\cdot\hat{\mathbf{D}}')\,[\,\cdot\,]\,d\rho' d\rho \\ &= \int_{\rho_L}^{\rho_U}\int_{\rho'_L}^{\rho'_U} \left(-\frac{\rho'\sin\alpha}{D_{CC'}}\right)\left(\frac{\rho\sin\alpha}{D_{CC'}}\right)[\,\cdot\,]\,d\rho' d\rho. \end{aligned} \tag{26}$$

With the choice

$$\frac{du'}{d\rho'} = \frac{\rho'\sin\alpha}{\sqrt{\rho^2 + \rho'^2 - 2\rho\rho'\cos\alpha}} = \frac{h'(\rho)}{D_{CC'}} = \cos\theta \tag{27}$$

the variation of the factor $\hat{\mathbf{u}}\cdot\hat{\mathbf{D}}$ in the line integral is canceled. Integration of (27) yields

$$u'(\rho,\rho') = \sin\alpha\, D_{CC'} + h\,(\rho)\cos\alpha\sinh^{-1}\left(\frac{\rho' - \rho\cos\alpha}{|h\,(\rho)|}\right). \tag{28}$$

Similarly, we can choose

$$\frac{du}{d\rho} = \frac{\rho\sin\alpha}{\sqrt{\rho^2 + \rho'^2 - 2\rho\rho'\cos\alpha}} = \frac{h(\rho)}{D_{CC'}} = \cos\theta', \tag{29}$$

where the derivation for u is dual to that for u' and the result (30) is obtained by merely exchanging unprimed and primed quantities, yielding

$$u(\rho,\rho') = \sin\alpha D_{CC'} + h'(\rho')\cos\alpha\sinh^{-1}\left(\frac{\rho - \rho'\cos\alpha}{|h'(\rho')|}\right). \tag{30}$$

For mapping the transcendental functions u' and u back to ρ' and ρ, the root-solving procedure described in [12] may be used. The inverse of the u' transform exists when the derivative $du'/d\rho'$ is non-vanishing, which, from (27), is the case except when $\rho' = 0$. However, this critical case occurs frequently for realistic triangle configurations. More generally, it happens when source and (rotationally projected) extended test segments intersect. If $\rho' = 0$ (the intersection point) is an extreme of the source segment, a different treatment of the line integral is required, as outlined below. If $\rho' = 0$ is an interior point, the domain needs to be divided into two sub-domains about the point $\rho' = 0$. Following the analysis of the behavior of u' near $\rho' = 0$ in [6], we must deal with a branch point at $\rho' = 0$, that can be removed via the transformation

$$v'^2 = \mathrm{sgn}(\sin\alpha)(u' - u'_0). \tag{31}$$

Similarly for u, a branch point at $\rho = 0$ is removed via the transformation

$$v^2 = \mathrm{sgn}(\sin\alpha)(u - u_0). \tag{32}$$

IV. Numerical Results

In this section, the numerical performance of the proposed approach is reported. We analyze the convergence behaviour of the contour and radial integrals separately. Hence, to study the convergence of one integral, we minimize the source of error due to the other integrals, calculating them with the highest accuracy we can achieve. The total number of quadrature points used for the different analysis is equal to $N_{comb}N_E^2N_{OR}N_{IR}$ where N_{comb} is the number of non-vanishing edge pair combinations ($N_{comb} \leq 9$), N_E represents the number of source/test edge quadrature points, N_{OR} is the number of quadrature points used for the outer radial integration, and N_{IR} is the number of quadrature points used for the inner radial integration. The reference values are obtained using the highest order Double Exponential (DE) quadrature scheme (90 points) for all the integrals [15], using quad precision and root-finding tolerances with precision comparable with the quadrature data; all reference values are accurate to no less than 16 significant digits. All displayed data is obtained using double precision.

In the vector potential reaction integrals, all nine linear (RWG) vector basis and testing function combinations are computed; error bars in the figures indicate the range of significant digits in the results for the nine vector potential reaction integrals. In the scalar/static potential quantities, the bases are constant hence a single result is reported. The maximum triangle edge length is fixed at 0.1λ, and the basis functions are standard RWG functions [16]. For each type of reaction integral considered, the number of significant digits (SD) of the evaluated integral is reported,

$$\mathrm{SD} = -\log_{10}(|(I_{\mathrm{ref}} - I_n)/I_{\mathrm{ref}}| + \delta), \tag{33}$$

where I_n and I_{ref} are the evaluated integrals with n sample points and with the highest number of sample points (reference) respectively. The term $\delta = 1.0\mathrm{E}{-16}$ is inserted in (33) in order to limit the precision to 16 digits (double precision). Two quadrature schemes, Gauss-Legendre (GL) and double exponential (DE), are considered to calculate the integrals.

The first analysis is a comparison between the two different radial integral transforms described in Sect. III-A. Fig. 8 reports the behaviour of scalar potential reaction integrals for a pair of edge-adjacent triangles having average edge lengths of $1\mathrm{m}$ and with an angle of 60° between them. The common edge case, with its two pairs of edges with touching endpoints, typically results in the largest error for non-coplanar triangle configurations. As previously discussed, the D'/R transform is able to evaluate the inner radial integral to machine precision using just one point, but only for static kernels (see Fig. 8.a), while the $1/R$ transform, though needing more points to achieve machine precision, nevertheless shows much better stability with respect to frequency (see Fig. 8.b). We only see a reduction of accuracy when the triangle edge lengths become larger than 0.1λ. Hence we only consider the $1/R$ transform in subsequent analyses.

To show the validity and applicability of the proposed method, we consider several triangle pairs configurations and different triangle shapes. Fig. 9 shows the behaviour of the

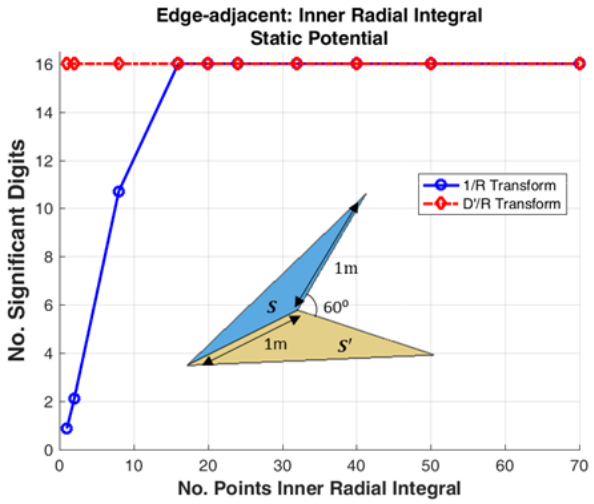

(a)

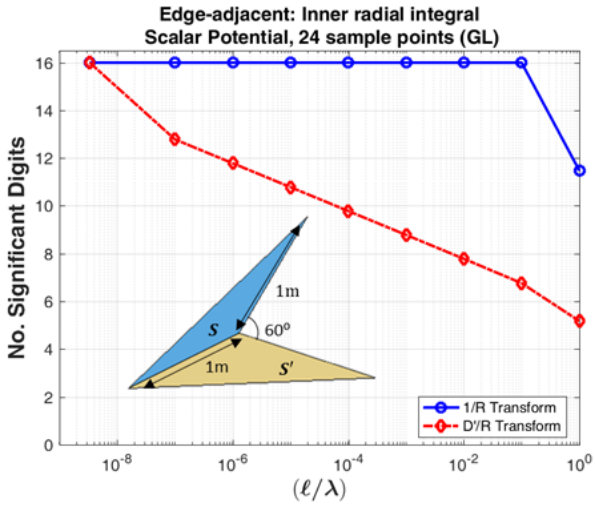

(b)

Fig. 8. Accuracy comparison between the two developed radial transforms; (a) static kernel vs. number of sample points; (b) scalar potential vs. triangle size vs. ℓ/λ where ℓ is the common edge length over wavelength ($N_{IR} = 24$ (GL)).

edge integrals for vector potential reactions for the same triangle configuration as in the previous analysis (see Fig. 9 (inset)). The scalar potential is not shown in the reported analyses because we verified that the number of correct significant digits is always 2 to 3 digits more with respect to the corresponding vector potential integral, as similarly observed in [6] for the coplanar case.

In order to concentrate on the behaviour of the edge integrals only, the radial integrals are calculated using a fixed GL scheme with 40 points for the inner radial integral and a DE quadrature rule with 90 points for the outer radial integral. For the inner radial integral the $1/R$ radial transform is used. Two quadrature schemes, GL and DE, with or without the edge transforms, are compared for an increasing number of quadrature sample points. The figure shows the number of correct significant digits with respect to the number of quadrature points per edge, that is the same for both edge integrals. As is typical of the DE scheme, GL shows better performance in low-to-medium accuracies, while the DE scheme is able to achieve very high accuracy. Moreover the integral accuracy is evaluated applying and not applying the proposed edge transforms. For the edge-adjacent case, since four of the interacting edge pairs are involved at each of the two common vertices, when the edge integral transforms u and u' are used, the v and v' transforms must also be used for each such edge pair (see Sect. III-B). The effectiveness of the edge integral transforms is evident: in the GL scheme, for a specified accuracy, the number of points needed is considerably reduced using the transforms, and, in the DE scheme, higher accuracy is achievable.

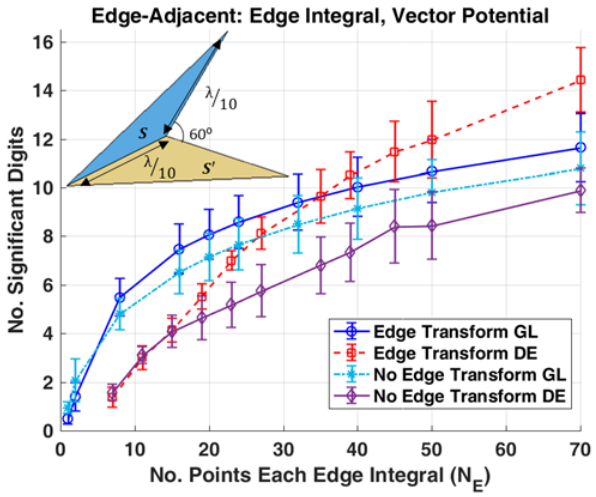

Fig. 9. Number of correct significant digits vs. number of sample points per edge; vector potential, edge-adjacent case for right isosceles triangle. Gauss-Legendre (GL) and double exponential (DE) quadrature rules with and without edge variable transforms are compared. The radial integrals are calculated with the highest accuracy available: $N_{OR} = 90$ DE, $N_{IR} = 40$ GL, and $N_{comb} = 6$. Error bars indicate the range of significant digits in the results for the nine vector potential reaction integrals.

Figure 10 shows, for the same set of triangles, the behaviour of the inner radial integral with increasing sample points both with and without use of the inner radial transform. The edge integrals and the outer radial integral are calculated with the highest order DE quadrature rule ($N_E = N_{OR} = 90$ points) to ensure the highest accuracy for these integrals. The effectiveness of the inner radial integral transforms is evident: in the GL scheme, without the variable transforms, we cannot achieve more than 8 significant digits, while, when using the inner radial transform, we are able to reach machine precision with fewer than 30 points.

Finally, in Fig. 11 convergence is analyzed for the outer radial integral for the same set of triangles. A very high order DE quadrature rule ($N_E = 90$ points) is used for the contour integrals. For the inner radial integral, a GL quadrature rule with $N_{IR} = 40$ points and the inner radial transform is used, since, as Fig. 10 shows, this is more than enough to reach machine precision for the inner radial integral. For the outer radial integral we compare the GL and DE schemes. As might be expected, the GL scheme appears more efficient at the lower accuracies, while for high accuracies the DE scheme is more effective.

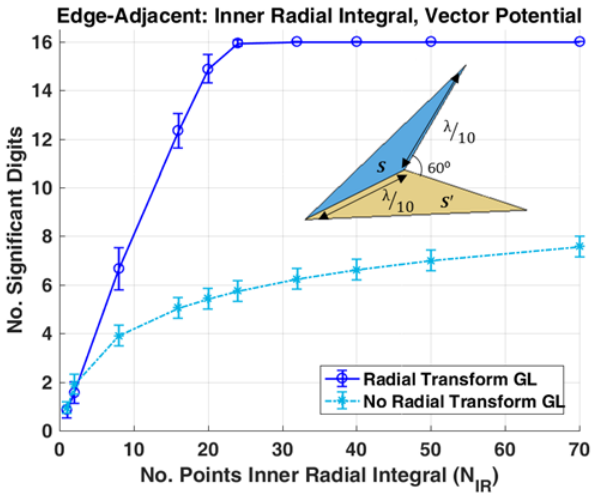

Fig. 10. Number of correct significant digits vs. number of sample points per inner radial integral; vector potential, edge-adjacent case for right isosceles triangle. Gauss-Legendre (GL) quadrature rule with and without inner radial variable transform are compared; the edge integrals and the outer radial integral are calculated with the highest accuracy available; $N_{OR} = 90$ DE and $N_E = 90$ DE, and $N_{comb} = 6$. Error bars indicate the range of significant digits in the results for the nine vector potential reaction integrals.

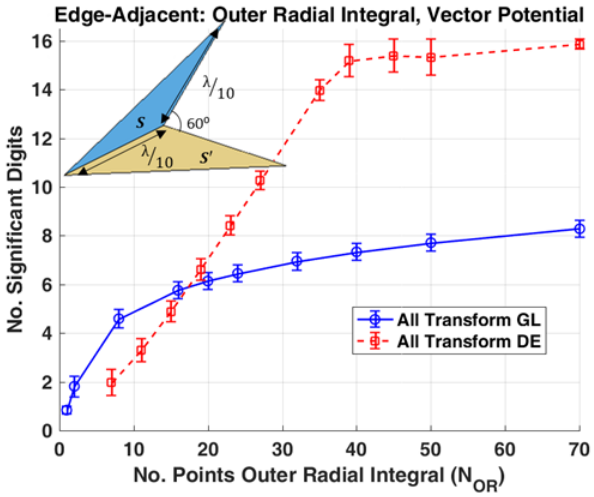

Fig. 11. Number of correct significant digits vs. number of sample points per outer radial integral; vector potential, edge-adjacent case for right isosceles triangle. Gauss-Legendre (GL), and double exponential (DE) quadrature rule with all variable transforms are compared; the edge integrals and the outer radial integral are calculated with the highest accuracy available; $N_{IR} = 40$ GL and $N_E = 90$ DE, and $N_{comb} = 6$. Error bars indicate the range of significant digits in the results for the nine vector potential reaction integrals.

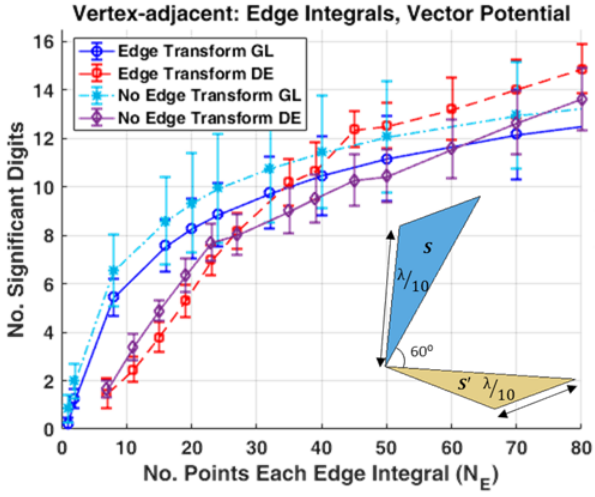

Fig. 12. Number of correct significant digits vs. number of sample points per edge; vector potential, vertex-adjacent case for two identical right isosceles triangles. Gauss-Legendre (GL) and double exponential (DE) quadrature rules with and without edge variable transforms are compared; the radial integrals are calculated with the highest accuracy available; $N_{OR} = 90$ DE and $N_{IR} = 40$ GL, and $N_{comb} = 6$. Error bars indicate the range of significant digits in the results for the nine vector potential reaction integrals.

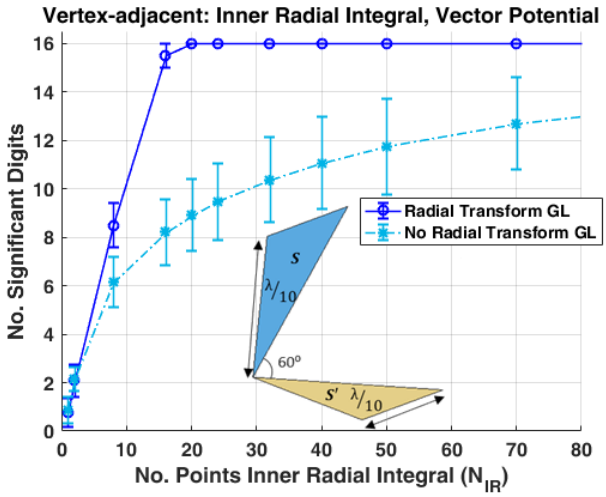

Fig. 13. Number of correct significant digits vs. number of sample points per inner radial integral edge; vector potential, vertex-adjacent case term case for two identical right isosceles triangles. Gauss-Legendre (GL) quadrature rule with and without inner radial variable transform are compared; the edge integrals and the outer radial integral are calculated with the highest accuracy available; $N_{OR} = 90$ DE and $N_E = 90$ DE, and $N_{comb} = 6$. Error bars indicate the range of significant digits in the results for the nine vector potential reaction integrals.

In Figs. 12–14 the same analysis is reported for vertex-adjacent triangles using the same triangles as for the edge-adjacent case, but positioned as shown in the corresponding insets. Convergence results for the edge integrals (Fig. 12) shows that the integrand is sufficiently smooth that GL quadrature rule provides almost 12 significant digits even without the edge integral transform. For the inner radial integral (Fig. 13), on the other hand, it is necessary to use the inner radial transform to reach machine precision. For the outer radial integral (Fig. 14), the GL scheme is more effective at achieving low accuracies, while the DE scheme is better for very high accuracies, as expected.

In Figs. 15–17, the same analysis is reported for a close but non-touching triangle pair as shown in the insets. In this case, high accuracy for the edge integrals (Fig. 15) is easily achieved using the GL quadrature rule without the need to apply the proposed edge transform; this result is to be expected since, with well-separated edge pairs, the integrand is smooth. For the inner radial integral, it is not even necessary to use the inner radial transform to reach machine precision with a low number of quadrature points. For the outer radial integral, the

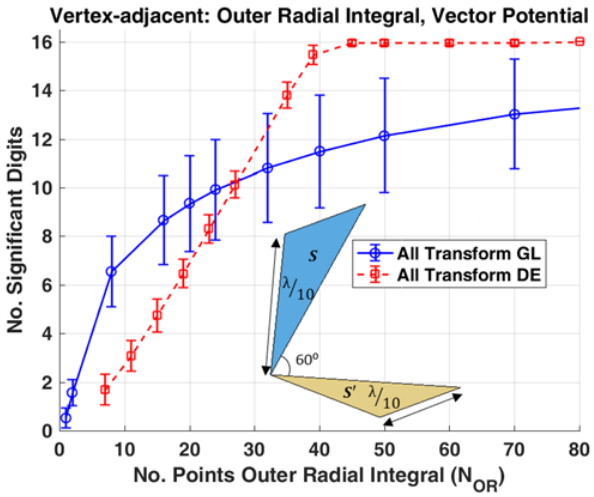

Fig. 14. Number of correct significant digits vs.number of sample points per outer radial integral edge; vector potential, vertex-adjacent case term case for two identical right isosceles triangles. Gauss-Legendre (GL) and double exponential (DE) quadrature rule with all variable transforms are compared; the edge integrals and the outer radial integral are calculated with the highest accuracy available; $N_{IR} = 40$ GL and $N_E = 90$ DE, and $N_{comb} = 6$. Error bars indicate the range of significant digits in the results for the nine vector potential reaction integrals.

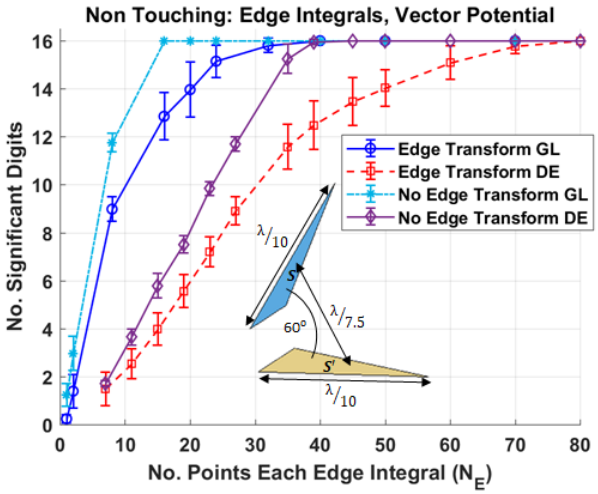

Fig. 15. Number of correct significant digits vs. number of sample points per edge; vector potential, non touching case term case for two identical right isosceles triangles. Gauss-Legendre (GL) and double exponential (DE) quadrature rules with and without edge variable transforms are compared; the radial integrals are calculated with the highest accuracy available; $N_{OR} = 90$ DE and $N_{IR} = 40$ GL, and $N_{comb} = 6$. Error bars indicate the range of significant digits in the results for the nine vector potential reaction integrals.

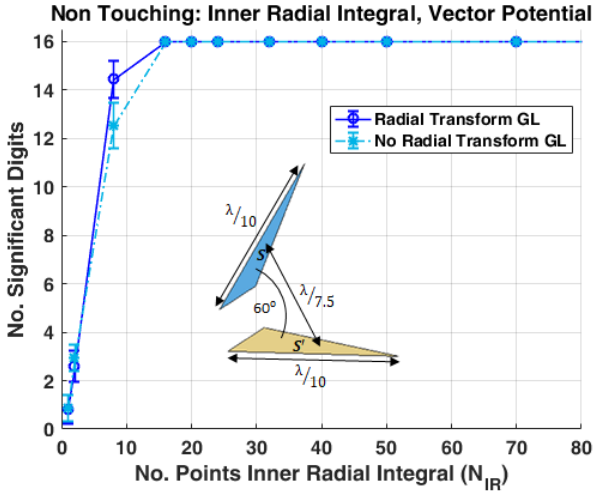

Fig. 16. Number of correct significant digits vs. number of sample points per inner radial integral edge; vector potential, non touching case for right isosceles triangles. Gauss-Legendre (GL) quadrature rules with and without inner radial variable transform are compared; the edge integrals and the outer radial integral are calculated with the highest accuracy available; $N_{OR} = 90$ DE and $N_E = 90$ DE, and $N_{comb} = 6$. Error bars indicate the range of significant digits in the results for the nine vector potential reaction integrals.

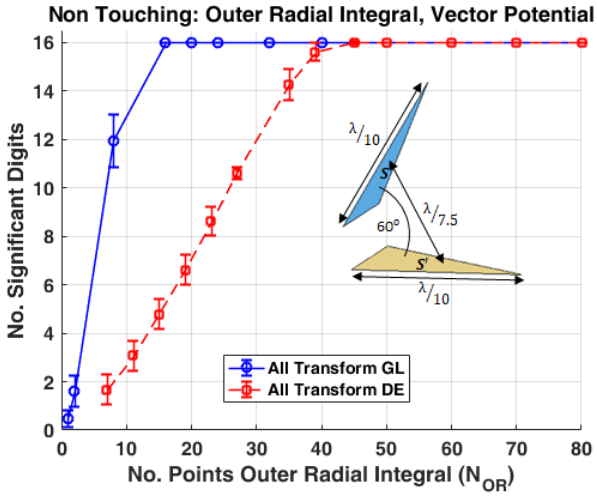

Fig. 17. Number of correct significant digits vs. number of sample points per outer radial integral edge; vector potential, non- touching case for two identical right isosceles triangles. Gauss-Legendre (GL) and double exponential (DE) quadrature rule with all variable transforms are compared; the edge integrals and the inner radial integral are calculated with the highest accuracy available; $N_{IR} = 40$ GL and $N_E = 90$ DE, and $N_{comb} = 6$. Error bars indicate the range of significant digits in the results for the nine vector potential reaction integrals.

GL scheme appears more effective for all accuracy ranges.

The contour plots in Fig. 18 show the number of correct significant digits for the edge-adjacent term in the case of a fixed equilateral test triangle whose edge length is $\lambda/10$ and for different-shaped source triangles. Rather than attempt to report 9 vector potential results for all the test and source bases, we report only the number of significant digits in scalar potential. They generally have very similar error characteristics, except the latter usually has about 2 more significant digits than the vector potential. The length of the adjacent edge is $\lambda/10$ while the remaining two edges of the source triangle assume all possible lengths $\leq \lambda/10$ [6]. The plot region is chosen so that the maximum length of the considered source triangle is always $\lambda/10$. The color of each point (x, y) represents the number of correct significant digits for a triangle with its third vertex at that point. For all integrals, the GL scheme with 16 quadrature points is used. In Fig. 18(a), all the proposed transforms are applied, whereas in Fig. 18(b), the reported results are obtained without transforms. As the figure illustrates, using transforms has the benefit of providing both

higher accuracy and less sensitivity to shape.

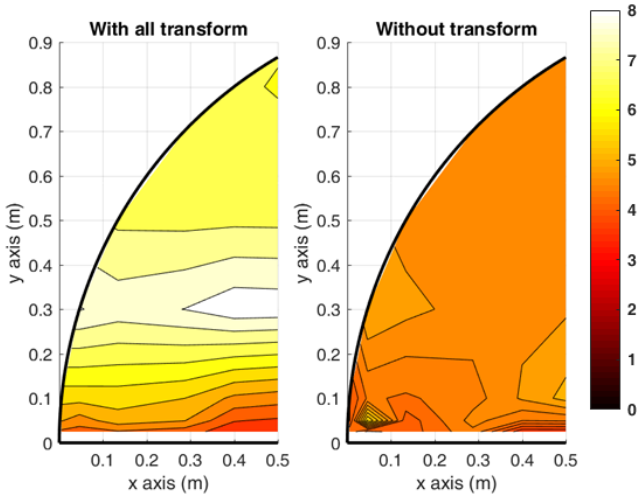

Fig. 18. Significant digits for scalar potential vs. triangle shape for an edge-adjacent triangle pair, one a fixed equilateral test triangle with vertices $\mathbf{r}_1 = (0, 0, 0)$, $\mathbf{r}_2 = (\sqrt{0.75}/2, 0.5, -0.75)$ and $\mathbf{r}_3 = (0, 1, 0)$ whose edge lengths are $\lambda/10$, and the second, a source triangle placed in the plane $z = 0$ with vertices at $\mathbf{r}'_1 = \mathbf{r}_1$ and $\mathbf{r}'_3 = \mathbf{r}_3$. The color at any point $(x, y, 0)$ locating vertex $\mathbf{r}'_2$ is keyed to the colorbar which indicates the number of correct significant digits for that triangle shape with (a) all transforms applied and (b) no transforms applied. The number of sample points per edge, per inner radial integral, and per outer radial integral are $N_E = N_{IR} = N_{0R} = 16$ (GL quadrature rule). For all the possible triangle configurations $N_{comb} \leq 8$. The plots are symmetric and only the left half of each is shown.

Finally, Fig. 19(a) reports the number of correct significant digits with respect to the total number of quadrature points used to evaluate the vector potential integral in the case of a pair of right isosceles triangles with a common edge and 60° angle between them. The scale at the top of Fig. 19(a) shows the average number of quadrature points along each of the four dimensions. The proposed scheme (blue line with circles, all transforms applied) is compared with the Radial-Angular (RA) singularity cancellation scheme applying the optimized approach described in [14] for source integration with a test integration performed using Gauss-Triangle quadrature (GT, red lines with star or diamond markers). The RA scheme is currently considered one of the most efficient source integral schemes [13]. To underscore here that in the RA results the limiting part is the test integral, its accuracy is also shown when the source quadrature rule used is increased by one point (RA opt+1, star markers); as seen, the additional sample points do not improve the accuracy. Fig. 19(b) presents the same data normalized with respect to CPU time. The normalized time reported is the time required to perform 100 evaluations of the 9 vector potential integrals divided by the time required for the same evaluation applying a simple GT quadrature scheme with 16 sample points for the traditional surface/surface test and source integrals.

It is also seen that the efficiency in terms of total number of points of the proposed method is similar to, but slightly less than that of the RA scheme. However, the number of quadrature points used in the RA scheme was optimized with respect to the subtriangle shape, whereas an optimized choice of the number of radial quadrature points has yet to

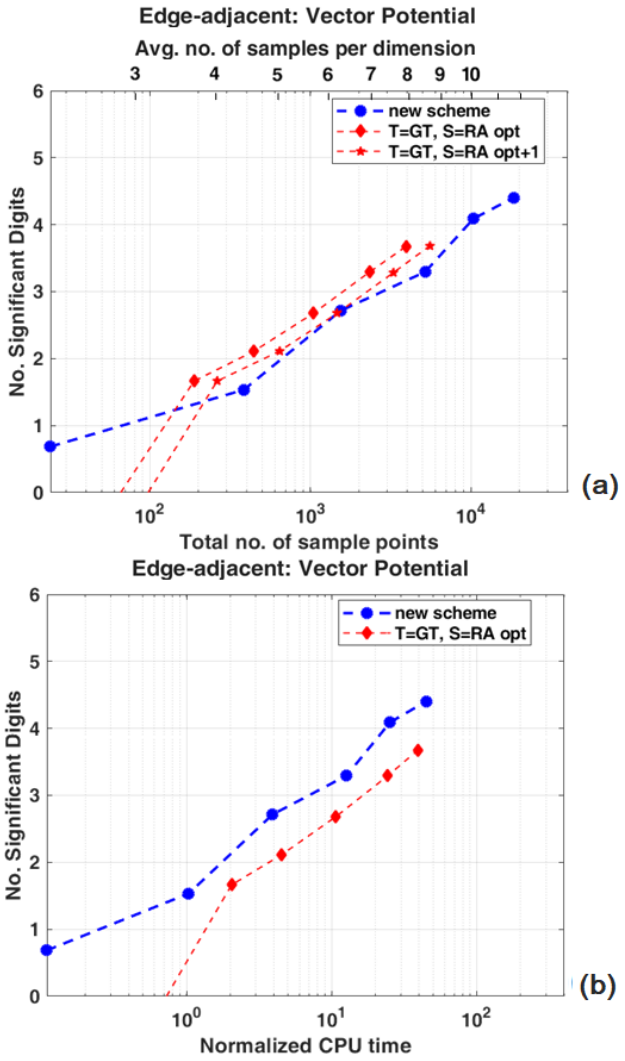

Fig. 19. Number of correct significant digits (a) vs. total no. of sample points and (b) vs. normalized time. Vector potential, edge-adjacent case for two identical right isosceles triangles whose perpendicular sides are of length $\lambda/10$ comparing the present scheme to the Radial-Angular (RA) singularity cancellation scheme [14] for the source triangle (S) using Gauss-Triangle (GT) quadrature scheme for the test integral (T). The scale at the top of (a) shows the average number of sample points along each of the four integration dimensions.

be developed for the present scheme. It may be possible to optimize the present scheme by extending the approach of the coplanar case [6] or perhaps using a quadrature error estimation approach as recently suggested in [17]. As for CPU time, despite being a more complex scheme, the proposed method performs slightly better than the RA scheme, most likely because our RA scheme first maps all sample points back to area coordinates and then the integral is evaluated in area coordinates. In any case, even without radial integral optimization, the proposed scheme has the advantage that it is fully compatible with that previously proposed for the coplanar case [6], which performs much better than competing schemes for triangle self-term evaluation.

For reference purposes, numerical values for tested scalar and vector potential integrals are provided in Table I. The coordinates of the vertices forming a pair of interacting

TABLE I
REFERENCE POTENTIALS FOR THE TRIANGLE PAIR WITH SOURCE TRIANGLE VERTICES $\mathbf{r}'_1 = (0,0,0)\text{m}$, $\mathbf{r}'_2 = (1,0,0)\text{m}$, $\mathbf{r}'_3 = (0,1,0)\text{m}$ AND TEST TRIANGLE VERTICES $\mathbf{r}_1 = \mathbf{r}'_1$, $\mathbf{r}_2 = \mathbf{r}'_3$, $\mathbf{r}_3 = (1/2, 0.0, \sqrt{3}/2)\text{m}$.

Static Potential		0.4544557923931120E-1		
Scalar Potential		0.4335390332088512E-1 -j0.1222853370574042E-1		
Vector Potential		Source Vertex Basis Function		
		1	2	3
Test Vertex Basis Function	1	0.1614666764741113E-1 -j0.4085167402404187E-2	0.3122307334298600E-2 -j0.1909037675592154E-4	-0.1059860793713104E-1 +j0.2882355758363133E-2
	2	-0.1059860793713104E-1 +j0.2882355758363134E-2	-0.1335987667815746E-1 +j0.4067218068873242E-2	0.2029187441021369E-1 -j0.6109683399476997E-2
	3	0.3122307334298598E-2 -j0.1909037675592152E-4	0.1801922721479905E-1 -j0.4098681021387152E-2	-0.1335987667815746E-1 +j0.4067218068873240E-2

triangles, T^e and T^f, members of an assumed element mesh of triangles $T^e, e = 1, 2, \ldots, E$, are, for source triangle T^f, $\mathbf{r}'_1 = (0,0,0)\text{m}$, $\mathbf{r}'_2 = (1,0,0)\text{m}$, $\mathbf{r}'_3 = (0,1,0)\text{m}$, and for test triangle T^e, $\mathbf{r}_1 = \mathbf{r}'_1$, $\mathbf{r}_2 = \mathbf{r}'_3$, and $\mathbf{r}_3 = (1/2, 0, \sqrt{3}/2)\text{m}$. The medium is free space and the wavenumber is $k = 2\pi/10$ ($\lambda = 10\text{m}$). RWG [16] functions $\mathbf{\Lambda}^f_j(\mathbf{r}')$ and $\mathbf{\Lambda}^e_i(\mathbf{r})$ are chosen as basis and testing functions $\mathbf{b}(\mathbf{r})$ and $\mathbf{t}(\mathbf{r})$, respectively. For scalar potential, the quantity computed in Table I is

$$\int_{T^e}\int_{T^f} \frac{e^{-jkR}}{4\pi R} dS'\, dS, \tag{34}$$

and for vector potential, the computed quantities are

$$\int_{T^e}\int_{T^f} \frac{e^{-jkR}}{4\pi R} \mathbf{\Lambda}^e_i(\mathbf{r})\mathbf{\Lambda}^f_j(\mathbf{r}')dS'\, dS, \;\; i,j = 1,2,3, \tag{35}$$

where the testing functions appearing in the vector potential are defined as

$$\mathbf{\Lambda}^e_i(\mathbf{r}) = \frac{\mathbf{r} - \mathbf{r}_i}{h_i}, \tag{36}$$

and where $\mathbf{r}_i$ is the vector to the ith vertex of T^e and h_i is that vertex's height above the opposite edge of triangle T^e; the jth basis function $\mathbf{\Lambda}^f_j(\mathbf{r}')$ on element T^f is similarly defined.

V. CONCLUSIONS

We propose a novel general formula for 4-D reaction integrals based on applying the surface divergence theorem to both test and source triangles, together with a reordering of the integration. The 4-D surface integrals are expressed as two radial integrals plus two contour integrals over source and observation domain boundaries. The method is numerically validated for static and dynamic kernels arising in the EFIE and linear basis functions. Moreover, it is directly applicable to basis functions of higher order. The method's efficiency, as represented by the number of correct significant digits for a chosen number of quadrature points, is improved by applying the proposed variable transformations for the edge and inner radial integrals. Moreover the proposed scheme shows reduced sensitivity to triangle shape.

The next step is to apply the proposed approach to other singular kernels. In particular, with suitable modifications, the scheme can also be applied to kernels with $\nabla(1/R)$ singularities. This objective will be addressed in a future study. Moreover the proposed approach can be extended to curved elements and volume integrals.

APPENDIX A
ROTATIONAL PROJECTION

We can describe mathematically the rotational projection, introduced in Sect. II-B, from an arbitrary axis and angle in terms of the following dyadic, as seen in [18]:

$$\boldsymbol{\mathcal{R}}(\hat{\mathbf{v}}, \beta) = \hat{\mathbf{v}}\hat{\mathbf{v}} + \sin\beta\,(\hat{\mathbf{v}} \times \boldsymbol{\mathcal{I}}) + \cos\beta(\boldsymbol{\mathcal{I}} - \hat{\mathbf{v}}\hat{\mathbf{v}}), \tag{37}$$

where $\hat{\mathbf{v}} = (\hat{v}_x, \hat{v}_y, \hat{v}_z)$ is a unit vector along the line of intersection of the two planes and can be defined as $\hat{\mathbf{v}} = (\hat{\mathbf{n}} \times \hat{\mathbf{n}}')/\|\hat{\mathbf{n}} \times \hat{\mathbf{n}}'\|$, where $\boldsymbol{\mathcal{I}}$ is the unit dyadic. Using (37) we can describe the projection of a point in the source plane $\mathbf{r}'_{C'} \in S'$ onto the test plane using the angle β as $\mathbf{r}'^0_{C'} = \mathbf{p}_0 + \boldsymbol{\mathcal{R}}(\hat{\mathbf{v}}, \beta)\cdot(\mathbf{r}'_{C'} - \mathbf{p}_0)$, where $\mathbf{p}_0$ is the point on the intersection axis closest to the origin,

$$\mathbf{p}_0 = \frac{(\mathbf{r}_{S'} \cdot \hat{\mathbf{n}}')}{||\hat{\mathbf{n}} \times \hat{\mathbf{n}}'||}(\hat{\mathbf{n}} \times \hat{\mathbf{v}}) - \frac{(\mathbf{r}_S \cdot \hat{\mathbf{n}})}{||\hat{\mathbf{n}} \times \hat{\mathbf{n}}'||}(\hat{\mathbf{n}}' \times \hat{\mathbf{v}}), \tag{38}$$

where $\mathbf{r}_{S'}$ is any point in S' and $\mathbf{r}_S$ is any point in S. Similarly, we define the projection of a point in the test plane $\mathbf{r} \in S$ onto the source plane as $\mathbf{r}^0 = \mathbf{p}_0 + \boldsymbol{\mathcal{R}}^T(\hat{\mathbf{v}}, \beta)\cdot(\mathbf{r} - \mathbf{p}_0)$, where $\boldsymbol{\mathcal{R}}^T(\hat{\mathbf{v}}, \beta)$ is the dyadic transpose, and can be expresed as $\boldsymbol{\mathcal{R}}^T(\hat{\mathbf{v}}, \beta) = \boldsymbol{\mathcal{R}}(\hat{\mathbf{v}}, -\beta)$.

REFERENCES

[1] A. G. Polimeridis, F. Vipiana, J. R. Mosig, and D. R. Wilton, "DIRECTFN: Fully Numerical Algorithms for High Precision Computation of Singular Integrals in Galerkin SIE Methods," *IEEE Transactions on Antennas and Propagation*, vol. 61, no. 6, pp. 3112–3122, Jun. 2013.

[2] A. G. Polimeridis and T. V. Yioultsis, "On the Direct Evaluation of Weakly Singular Integrals in Galerkin Mixed Potential Integral Equation Formulations," *IEEE Transactions on Antennas and Propagation*, vol. 56, no. 9, pp. 3011–3019, Sep. 2008.

[3] A. G. Polimeridis and J. R. Mosig, "Complete Semi-analytical Treatment of Weakly Singular Integrals on Planar Triangles via the Direct Evaluation Method," *Int. J. Numer. Meth. Engng.*, vol. 83, no. 12, pp. 1625–1650, Sep. 2010. [Online]. Available: http://onlinelibrary.wiley.com/doi/10.1002/nme.2877/abstract

[4] A. G. Polimeridis, J. M. Tamayo, J. M. Rius, and J. R. Mosig, "Fast and Accurate Computation of Hypersingular Integrals in Galerkin Surface Integral Equation Formulations via the Direct Evaluation Method," *IEEE Transactions on Antennas and Propagation*, vol. 59, no. 6, pp. 2329–2340, Jun. 2011.

[5] A. G. Polimeridis and J. R. Mosig, "On the Direct Evaluation of Surface Integral Equation Impedance Matrix Elements Involving Point Singularities," *IEEE Antennas and Wireless Propagation Letters*, vol. 10, pp. 599–602, 2011.
[6] D. Wilton, F. Vipiana, and W. Johnson, "Evaluation of 4-D Reaction Integrals in the Method of Moments: Co-planar Element Case," *IEEE Transactions on Antennas and Propagation*, vol. 65, no. 5, pp. 2479–2493, May 2017.
[7] D. Wilton, S. Rao, A. Glisson, D. Schaubert, O. Al-Bundak, and C. Butler, "Potential Integrals for Uniform and Linear Source Distributions on Polygonal and Polyhedral Domains," *IEEE Transactions on Antennas and Propagation*, vol. 32, no. 3, pp. 276–281, Mar. 1984.
[8] L. Knockaert, "On the Analytic Calculation of Multiple Integrals in Electromagnetics," in *2011 International Conference on Electromagnetics in Advanced Applications*, Sep. 2011, pp. 595–598.
[9] P. Arcioni, M. Bressan, and L. Perregrini, "On the Evaluation of the Double Surface Integrals Arising in the Application of the Boundary Integral Method to 3-D Problems," *IEEE Transactions on Microwave Theory and Techniques*, vol. 45, no. 3, pp. 436–439, Mar. 1997.
[10] D. Tihon and C. Craeye, "Closed-form Evaluation of the Singular Terms in Electric Field Integral Equations," in *The 11th European Conference on Antennas and Propagation*, Paris, France, 2017, pp. 520–524.
[11] J. Rivero, F. Vipiana, D. R. Wilton, and W. A. Johnson, "Acceleration of 4-D Reaction Integrals in the Method of Moments via Double Application of the Divergence Theorem and Variable Transformations," in *The 11th European Conference on Antennas and Propagation*, Paris, France, Mar. 2017.
[12] F. Vipiana and D. R. Wilton, "Numerical Evaluation via Singularity Cancellation Schemes of Near-Singular Integrals Involving the Gradient of Helmholtz-Type Potentials," *IEEE Transactions on Antennas and Propagation*, vol. 61, no. 3, pp. 1255–1265, Mar. 2013.
[13] M. M. Botha, "Accuracy of Near-Singularity Cancellation Quadrature Schemes for the Dynamic MoM Kernel," *IEEE Antennas and Wireless Propagation Letters*, vol. 12, pp. 714–717, 2013.
[14] M. A. Khayat, D. R. Wilton, and P. W. Fink, "An Improved Transformation and Optimized Sampling Scheme for the Numerical Evaluation of Singular and Near-Singular Potentials," *IEEE Antennas and Wireless Propagation Letters*, vol. 7, pp. 377–380, 2008.
[15] A. G. Polimeridis, I. D. Koufogiannis, M. Mattes, and J. R. Mosig, "Considerations on Double Exponential-Based Cubatures for the Computation of Weakly Singular Galerkin Inner Products," *IEEE Transactions on Antennas and Propagation*, vol. 60, no. 5, pp. 2579–2582, May 2012.
[16] S. Rao, D. Wilton, and A. Glisson, "Electromagnetic Scattering by Surfaces of Arbitrary Shape," *IEEE Transactions on Antennas and Propagation*, vol. 30, no. 3, pp. 409–418, May 1982.
[17] M. M. Botha and T. Rylander, "Quadrature Error Estimation for MoM Matrix Entries," in *The International Conference in Electromagnetics and Advanced Applications*, Verona, Italy, 2017, pp. 973–975.
[18] I. V. Lindell, *Methods for Electromagnetic Field Analysis*. New York: IEEE Press Series on Electromagnetic Wave Theory, 2000.

Javier Rivero received the M.S. Telecommunication Engineering degree at University Carlos III de Madrid, Spain in 2008 and the Ph.D. in Telecommunication Engineering from University of Extremadura, Spain in 2012. From 2012 to 2017 he was a research assistant at the Department of Technologies of Computers and Communications at University of Extremadura, Spain. From 2015 to 2017 he did a postdoctoral stay at the Department of Electronics and Telecommunications of Politecnico di Torino. From 2017 to 2018 he was at the Advanced Computing and Electromagnetics (ACE) of Istituto Superiore Mario Boella (ISMB). Since 2018, he has been a research assistant with the Department of Electronics and Telecommunications, Politecnico di Torino.

His current research interests include fast integral-equation methods and method of moment approaches in computational electromagnetics, metamaterials, nanoplasmonics, Greens function regularization, and advanced quadrature integration schemes.

Francesca Vipiana (M'07–SM'13) received the Laurea and Ph.D. degrees in electronic engineering from the Politecnico di Torino, Torino, Italy, in 2000 and 2004, respectively, with doctoral research carried out partly at the European Space Research Technology Center, Noordwijk, The Netherlands. From 2005 to 2008, she was a Research Fellow with the Department of Electronics, Politecnico di Torino. From 2009 to 2012, she was the Head of the Antenna and EMC Lab with the Istituto Superiore Mario Boella, Torino. Since 2012, she has been an Assistant Professor with the Department of Electronics and Telecommunications, Politecnico di Torino, where she has been an Associate Professor since 2014. Her current research interests include numerical techniques based on the integral equation and method of moment approaches, with a focus on multiresolution and hierarchical schemes, domain decomposition, preconditioning and fast solution methods, and advanced quadrature integration schemes. Prof. Vipiana received the Young Scientist Award at the URSI General Assembly in 2005, the first prize in the poster competition at the IEEE Women in Electromagnetics Workshop in 2009, the ISMB Best Paper Award in 2011, and the Lot Shafai Mid-Career Distinguished Award from the IEEE Antennas and Propagation Society in 2017.

Donald R. Wilton (S'63–M'65–SM'80–F'87–LF'08) received the B.S., M.S., and Ph.D. degrees in Electrical Engineering from the University of Illinois, Urbana-Champaign, in 1964, 1966, and 1970, respectively. From 1965 to 1968 he was with Hughes Aircraft Co., Fullerton, CA, engaged in the analysis and design of phased array antennas. From 1969 to 1970, he pursued the Ph.D. under a Hughes Doctoral Fellowship. From 1970–1983 he was with the Department of Electrical Engineering, University of Mississippi. He was a Visiting Professor at Syracuse University during the academic year 1978–1979. He was with the University of Houston from 1983 until 2012, retiring as Professor Emeritus in the Department of Electrical and Computer Engineering. During the 2004–2005 academic year he was a visiting professor at the Polytechnic of Turin, Italy, Sandia National Laboratories, and the University of Washington. His primary research area is computational electromagnetics, and he has published, lectured, and consulted extensively in this area. Dr. Wilton is a Life Fellow of the IEEE and received the IEEE Third Millennium Medal. He has served the IEEE Antennas and Propagation Society as an Associate Editor of the Transactions on Antennas and Propagation, as a Distinguished National Lecturer, and as a member of its Administrative Committee. He is also a member of URSI Commission B, in which he has held various offices, including Chair of US Commission B. Dr. Wilton received the ACES inaugural Computational Electromagnetic Award in 2013, the IEEE Antenna and Propagation Society's inaugural Harrington-Mittra Award in Computational Electromagnetics in 2014, and the 2015 IEEE Electromagnetics Award.

William A. Johnson (M'00–SM'02) received the B. S., M. A., and Ph. D. degrees in mathematics with minors in physics from the University of Arizona, Tucson, AZ, in 1972, 1974, and 1978, respectively. The Ph. D. degree was obtained in association with the Interdisciplinary Applied Math program at the University of Arizona. He is the author/co-author of 41 journal articles. His work experience includes Sandia National Laboratories, Lawrence Livermore National Laboratory, University of Mississippi, and adjunct associate professor of mathematics at the University of New Mexico. He was a visiting assistant professor of mathematics at New Mexico Institute of Mining and Technology, in Socorro New Mexico for the 2016-2107 academic year. Dr. Johnson is a full member of URSI Commission B and a Senior Member of the IEEE. New Mexico Tech is gratefully acknowledged for providing this photo.